ISA Transactions 147 (2024) 153–162

Contents lists available at ScienceDirect

ISA Transactions

journal homepage: www.elsevier.com/locate/isatrans

Research article

Quantifying the performance enhancement facilitated by fractional-order implementation of classical control strategies for nanopositioning ☆

Tiecheng Wang [a,b], Andres San-Millan [c,*], Sumeet S. Aphale [c]

[a] Tianjin University of Technology and Education, Tianjin 300222, PR China
[b] Tangshan Polytechnic College, Tangshan 063299, PR China
[c] Artificial Intelligence, Robotics and Mechatronic Systems Group (ARMS), School of Engineering, University of Aberdeen, Aberdeen, AB24 3UE, UK

ARTICLE INFO

Keywords:
Fractional order control
Nanopositioning
Piezoelectric actuators
Robust control

ABSTRACT

For most nanopositioning systems, maximizing positioning bandwidth to accurately track periodic and aperiodic reference signals is the primary performance goal. Closed-loop control schemes are employed to overcome the inherent performance limitations such as mechanical resonance, hysteresis and creep. Most reported control schemes are integer-order and combine both damping and tracking actions. In this work, fractional-order controllers from the positive position feedback family namely: the Fractional-Order Integral Resonant Control (FOIRC), the Fractional-Order Positive Position Feedback (FOPPF) controller, the Fractional-Order Positive Velocity and Position Feedback (FOPVPF) controller and the Fractional-Order Positive, Acceleration, Velocity and Position Feedback (FOPAVPF) controller are designed and analysed. Compared with their classical integer-order implementation, the fractional-order damping and tracking controllers furnish additional design (tuning) parameters, facilitating superior closed-loop bandwidth and tracking accuracy. Detailed simulated experiments are performed on recorded frequency-response data to validate the efficacy, stability and robustness of the proposed control schemes. The results show that the fractional-order versions deliver the best overall performance.

1. Introduction

Nanopositioning systems are used for a variety of applications requiring precise positioning at nanometer resolution. Piezoelectric actuators (PEAs) are widely used in nanopositioning systems (both platform-type and tube-type) due to advantages of fast response, high resolution, repeatability, ease of integration and, the absence of friction and stiction. However, the mechanical resonance and nonlinear effects such as creep and hysteresis impose significant limitations on the system's ability to achieve precise positioning, [1,2]. Several control strategies have been reported in literature to overcome these severe performance limits, [3–7]. The common approach is to devise a control scheme that combines both damping (for mechanical resonance) and tracking (for minimizing errors due to nonlinearities) actions, [8].

To improve the positioning performance of nanopositioners, the most effective and commonly used closed-loop control technique is the simultaneous execution of two control loops, combining damping and tracking, also known as simultaneous damping and tracking control. This composite control algorithm based on the principle of feedback regulation can be applied in piezoelectric materials or similar structures. The inner loop of this control algorithm consists of a suitable damping controller, which provides a large amount of damping for the main resonant mode. The outer loop consists of a simple integral tracker in order to provide reference tracking. As a result, it becomes easier to apply a high gain tracking controller, which reduces positioning errors arising from nonlinear effects like hysteresis and creep [9]. For damping loops, any controller can be selected; using positive position feedback (PPF) [10], positive velocity and position feedback (PVPF) [11], integral resonance control (IRC) [12] and positive acceleration, velocity and position feedback (PAVPF) [13].

All of the above control strategies are effective in suppressing external disturbances; however recent research has demonstrated that simultaneous design of damping and tracking control strategies produce more robust controllers [14] and leads to much better positioning performance across a wider range of frequencies [15,16], as well as facilitating the stabilization of these type of Negative imaginary (NI) systems by means of a dissipative action [17].

☆ This research was partially supported by 'The Excellent Going Abroad Experts' Training Program in Hebei Province' and partially by the Aberdeen Grants Academy with the Pump-Prime award CF10723-44.

* Corresponding author.
E-mail address: andres.san-millanrodriguez@abdn.ac.uk (A. San-Millan).

https://doi.org/10.1016/j.isatra.2024.01.033
Received 30 April 2023; Received in revised form 5 December 2023; Accepted 28 January 2024
Available online 30 January 2024

Although simultaneous design of damping and tracking has demonstrate to produce an increment of the available bandwidth while maintaining a flat frequency response, there are still limitations associated to the use of a single integral action in the tracking controller such as (a) the tracking error of ramp references can only be reduced by increasing the tracking gain (b) using a second order integral action in the tracking controller modifies drastically the phase margin in the system and may lead to unstable behaviour. These limitations motivate the proposed work, it has been demonstrated that using a fractional-order integral action in the tracking controller may lead to better performance in terms of bandwidth and tracking for some control schemes [18], that is why this works aims to quantify the increase in performance achieved by the fractional-order implementation of some of the most well-known control schemes for nanopositioning systems, namely IRC, PPF, PVPF and PAVPF.

The advent of fractional-order calculus in recent years has allowed the traditional integer-order differential model and controller to be transitioned to a non-integer-order model and controller respectively. In recent years, fractional order dynamic models and controllers have been proposed [19–26]. Fractional-order controllers are typically employed to create robust control strategies by establishing phase margins for closed-loop systems [27,28] and are widely used in intelligent structural control with vibration problems as the main content [29–31]. Fractional order calculus has demonstrated superior performance for both higher achievable bandwidth and low output errors in the field of nanopositioning [18,32–35] at least theoretically.

The key contribution of this work is the detailed performance comparison of the integer-order and fractional-order implementations of four popular control schemes that combine both damping and tracking actions and are employed in control of nanopositioning systems. These control schemes combine one of the four damping controllers viz: Integral Resonant Control (IRC), the Positive Position Feedback (PPF) controller, the Positive Velocity and Position Feedback (PVPF) controller and the Positive, Acceleration, Velocity and Position Feedback (PAVPF) with a suitably gained integrator for tracking. Controller design, tracking gain selection, stability analysis and performance quantification employing measured frequency response data is presented. As the system is well-studied, accurate models of the open-loop system are established and facilitate controller designs. Closed-loop performance is then simulated using the measured frequency response data in a series of *simulated experiments*.

The following is an outline of how the paper is organized: Section 2 presents a brief description of the experimental setup used to record the relevant frequency response data used in the design, analysis and experiments presented in this paper. It then briefly presents the system model. Section 3 discusses the design and stability of the four classical control schemes in their integer-order form. Section 4 presents the fractional-order design for the four classical controllers named FOIRC, FOPPF, FOPVPF and FOPAVPF, in detail. Section 5 presents the comparative closed-loop results both in time- and frequency domain and then continues to quantify the closed-loop positioning performance of each control scheme. Section 6 concludes the paper.

2. System modelling

The behaviour of a piezo-actuated nanopositioning stage that is guided by a flexure hinge can be described using a mathematical model that involves an infinite number of second-order systems, each characterized by lightly damped resonant modes:

$$G_M(s) = \sum_{i=1}^{M} \frac{\sigma_i^2}{s^2 + 2\zeta_i\omega_i s + \omega_i^2} \tag{1}$$

in the transfer function, M represents the number of vibration modes that are taken into account, and it is desirable that M approaches infinity. The term σ_i^2 denotes the gain of each individual vibration mode, while ζ_i represents the damping ratio of each mode, and ω_i corresponds to the natural frequency of vibration of each mode

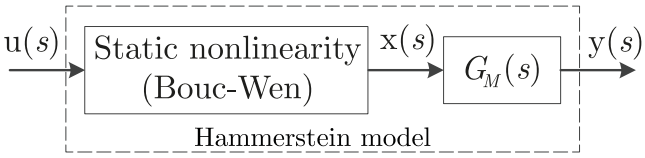

Fig. 1. Hammerstein model structure of the nanopositioner.

Additionally to the linear behaviour of the system, there are some important nonlinear effects due to the presence of PEAs. Traditionally, hysteresis is considered as the most significant effect and can be modelled together with the linear dynamics in the form of an Hammerstein system as in [36] where a static nonlinearity is placed in series preceding the linear dynamic part of model. This representation accounts for the rate-dependent curves of the hysteresis of the system at high frequencies.

In order to reproduce the hysteretic behaviour of the system, the Bouc–Wen model of hysteresis has been used in this paper as the nonlinear part of the Hammerstein representation, leading to the structure is shown in Fig. 1 as the complete representation of the nanopositioner. It can be seen that the Hammerstein representation has its correspondence with the physical system where the voltage applied to the piezoelectric actuators produces a deformation of the piezoelectric crystal, and thus a displacement of the tip of the actuator, x, and the displacement of the tip of the actuator produces a force on the mechanical compliant system that determines the displacement of the end effector of the nanopositioner, y. This arrangement provides a direct explanation of the two main dynamics involved, i.e. hysteretic behaviour due to the PEAs and a second order dynamics because of the elasticity of the complaint mechanism that behaves like a mass–spring–damper system.

2.1. Experimental setup

The experimental arrangement depicted in Fig. 2 is a nanopositioner that was developed at EasyLab. This nanopositioner consists of a flexure-based XY serial mechanism that is actuated by two PZT stacks, and it is capable of delivering a displacement of up to 20 μm. To drive the PZT actuators, two piezoelectric amplifiers are employed. These amplifiers increase the control signal voltage by a gain factor of 20 and add a bias term of 100 V. The nanopositioner can provide translational motion in space which is measured using a Microsense 4810 capacitive displacement sensor and a 2805 measurement probe. The measurement probe has a measurement range of ±50 μm, corresponding to a voltage output of ±10 V. In order to interface between the experimental platform and the control design, a PCI-6621 data acquisition card from National Instruments is used. The data acquisition card is connected to a PC that runs the Real-Time Module from LabVIEW. The PC used in the experiment is an OPTIPLEX 780, equipped with an Intel(R) Core(TM)2 Duo Processor running at 3.167 GHz and 2 GB of DDR3 RAM memory. The system is capable of achieving deterministic sampling times as low as 30×10^{-6} s.

2.1.1. Linear dynamics subsystem

To obtain the open-loop frequency response data for one axis of the nanopositioner, small signal frequency response functions (FRFs) are employed. This involves applying a sinusoidal chirp signal (with a small amplitude of 0.2 V) as input to the nanopositioner over a frequency range of 0.1 to 1800 Hz. The input and output signals are then used to compute the FRFs by taking the Fourier transform of the recorded data. It is important to note that the use of small amplitudes ensures that the nonlinear effects of the piezoelectric actuators (PEAs), such as hysteresis, can be neglected [37].

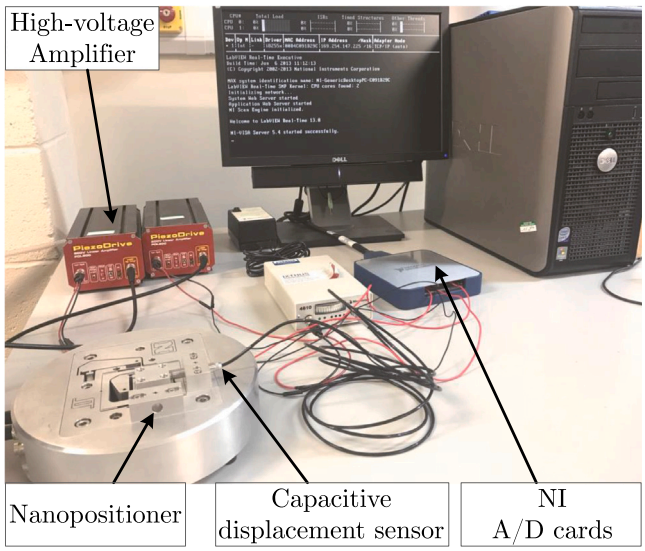

Fig. 2. Two-axis nanopositioner (EasyLab, University of Nevada, Reno) driven by PiezoDrive 200 V linear voltage amplifiers and measured by a Microsense 4810 capacitive sensor.

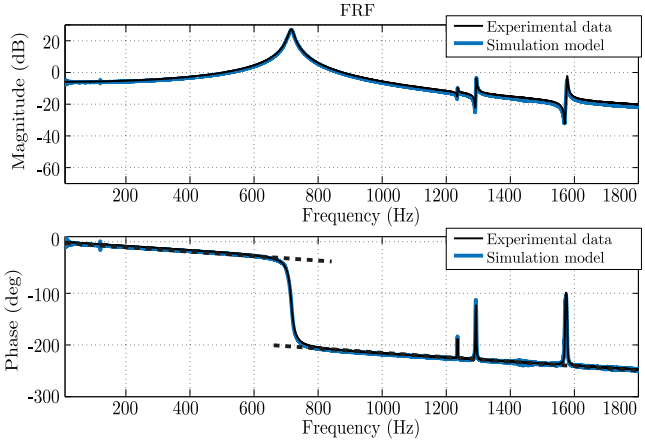

Fig. 3. Experimental platform's input-to-output displacement FRF.

Table 1
Identified values of the linear dynamics of the nanopositioner.

Harmonic	$\omega_i = 2\pi f_i$	ζ_i	σ_i
1st	$2\pi \times 716.2$	0.011	3200
2nd	$2\pi \times 1235.5$	0.0005	100
3rd	$2\pi \times 1294$	0.0008	250
4th	$2\pi \times 1578$	0.0008	350

Fig. 3 shows the recorded amplitude–frequency characteristic curve plotted for a sampling time of 50×10^{-6} s. It can be seen that 4 modes of vibration have been identified with a high degree of accuracy, the parameters of the four modes according to expression (1) are showed in Table 1

Note that the linear dynamic model (transfer-function) is only used during controller design. The simulated experiments as presented in Section 5 are performed using the measured frequency response data.

2.1.2. Hysteresis subsystem

A rate-dependent hysteresis system is a system where the output depends not only on the current input signal but also on the previous input signals and their frequency. As shown in Fig. 4(a), the nanopositioner have rate-dependent hysteresis, i.e, when the input signal is of high frequency, the input–output relationship is different to the response at low frequencies. To address this issue the FRF obtained in the identification of the linear part of the system is used to compensate for the magnitude and phase of the linear part of the system. After the compensation of the linear dynamics, the input–output relationship is the one showed in Fig. 4(b). It can be seen that after the compensation the hysteresis cycle is the same for all the excitation frequencies.

Because of the symmetric hysteresis loops showed in Fig. 4(b), the Coleman–Hodgdon model is chosen to model the hysteresis of the experimental platform [38].

The Coleman–Hodgdon hysteresis model can be defined in the form of the first order nonlinear differential equation in the time domain as follows:

$$\dot{y} = f(u, y)|\dot{u}| + g(u, y)\dot{u} \tag{2}$$

where y is the output and u is the input of the hysteresis model. Both y and u are real-valued functions of time with piecewise continuous derivatives, $\dot{y}$ and $\dot{u}$.

The above described equation can be used for a broad class of hysteretic systems by an appropriate choice of the functions $f(\cdot)$ and $g(\cdot)$. In this paper the following functions is chosen:

$$\dot{y} = |\dot{u}|(\gamma u - \alpha y) + \beta\dot{u} \tag{3}$$

where the parameters α, β and γ are obtained from experimentally by minimizing the error between the output of the theoretical model and the experimental data when the same input signal is applied to the system. The identified parameters were: $\alpha = 0.84$, $\beta = 1.068$ and $\gamma = 1.26$. It can be seen from Fig. 5 that there is a good fit between experiments and the identified model. The experimental data showed in Fig. 5 was obtained at a low frequency (1 Hz) in order to eliminate the effects of the linear part of the system that were more relevant at frequencies starting from 100 Hz.

3. The classical control schemes

This section introduces four classical control schemes that have been successfully applied in the past to control nanopositioning systems: the IRC, PPF, PVFP and PAVPF controllers. Among the methods available in scientific literature, these have been selected based on the following characteristics: (1) they yield simple controllers, (2) they are robust to spillover, (3) they can provide a maximally flat magnitude response while maximizing the closed-loop bandwidth considering the well-known criterion of ±3 dB, and (4) their stability is robust to large variations in the plant parameters and the presence of disturbances. The main focus of this paper is on properties (3) and (4), and it has been determined that these methods are the most suitable for achieving these objectives.

The previous control techniques share in common their structure, which is composed by two well-differentiated control stages: the first one is a inner control loop, usually called damping controller, $C_d(s)$, whose main objective is to damp the low frequency vibration modes of the system. The second control loop, called tracking controller $C_t(s)$, acts over the damped system and it allows to different track reference signals.

In [39], explicit formulas are provided to adjust the three controllers mentioned above in order to achieve a closed-loop magnitude response that is maximally flat. Even though the explicit expressions provide a good performance in terms of closed-loop bandwidth, in order to carry out a fair comparison between the classical integer-order regulators and the proposed fractional-order versions, the parameters of these regulators will be obtained by means of an optimization procedure where closed-loop frequency response is the maximization goal and, the closed-loop stability of the system and a flat band response contained in the ±2 dB band are considered as restriction. By doing so, all the regulators and their closed-loop bandwidth can be compared under the same design conditions.

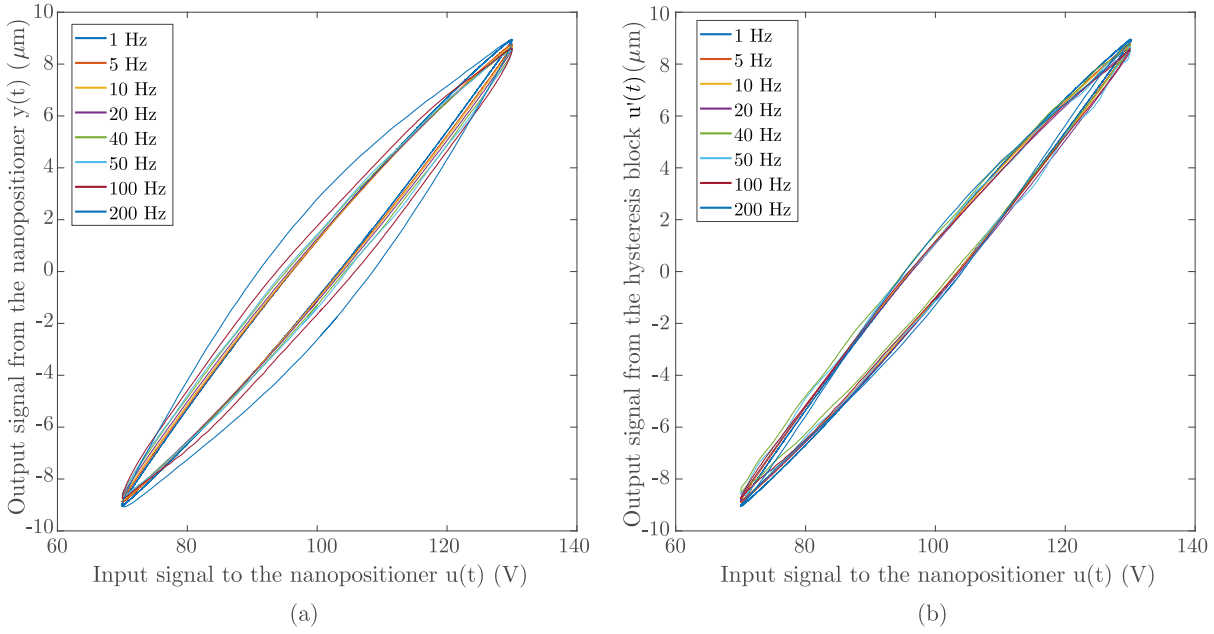

Fig. 4. Hysteresis curves of the nanopositioning platform. (a) Rate-dependent hysteresis characteristics of the complete system and (b) Rate-independent hysteresis characteristics of the piezoelectric actuator (PEA) after phase and magnitude compensation of the linear dynamics of the system.

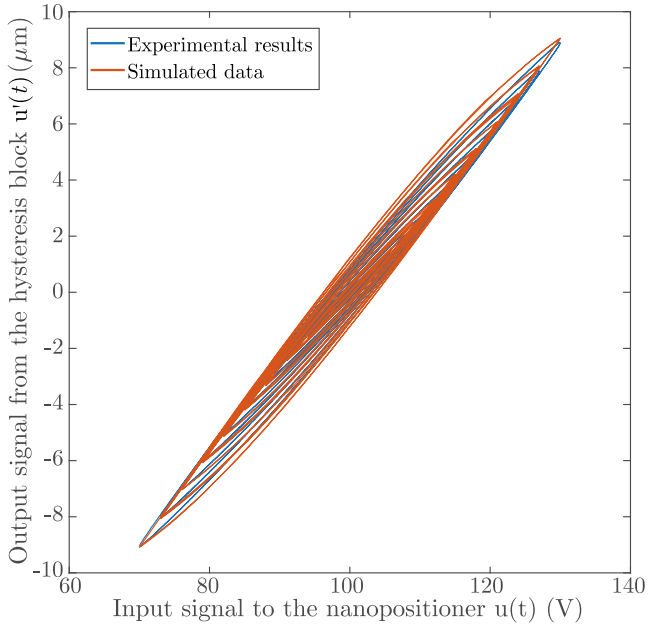

Fig. 5. The input and output curves of the experimental and simulated system when the input signal frequency is 1 Hz.

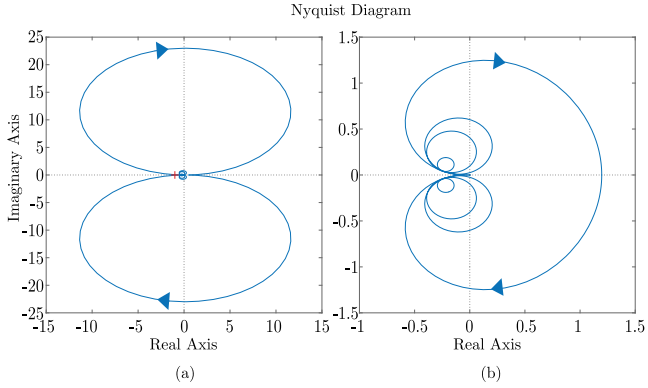

Fig. 6. Nyquist diagram of (a) the open-loop system and, (b) the open-loop system + the damping controller.

From the point of view of the frequency response, the four control schemes (IRC, PPF, PVPF and PAVPF) share the same approach in the control of the nanopositioning systems, first the damping controller is designed so that the low-frequency vibration mode of the system (the first resonant mode) is highly damped and, then the tracking controller provides an integral action so that the closed-loop response can track arbitrary references. This damping effect can be seen in Fig. 6 where the open loop Nyquist diagram is showed for the identified parameters of Table 1 (a) and compared with the effect of the system when the damping controller is applied (b), It can be seen in (a) that the first vibration mode is clearly dominant and after the application of the damping controller its amplitude is highly reduced (b). Additionally it can be seen that the second and higher modes are much smaller than the first one and they do not destabilize the closed-loop response.

The effect of the tracking controller over the Nyquist diagram of the system is to introduce a rotation of 90° clockwise so that there is an asymptote as showed in Fig. 7. It can be seen that the stability of the system and the robustness to perturbations is determined to the phase margin ϕ. The phase margin is determined by the parameters of the controller (that will determine the point where the Nyquist plot crosses the unit circle) and the overall shape of the Nyquist plot. As all the classical controllers share in common the integral action of the tracking controller, the overall shape of the Nyquist plot will be the same for all of them.

Because of the high value of the phase margin ϕ, all the classical controllers are very robust to external perturbations, however, since the tracking controller is composed of a single integrator, these controllers are effective in tracking step signals without steady-state error, as shown in [39]. However, they are not capable of tracking ramp or triangular signals without a constant tracking error. Since triangular signals are commonly used in atomic force microscopes (AFMs), where one axis of the nanopositioner is actuated with a triangular signal and the other with a slow-moving ramp during raster scanning, improving

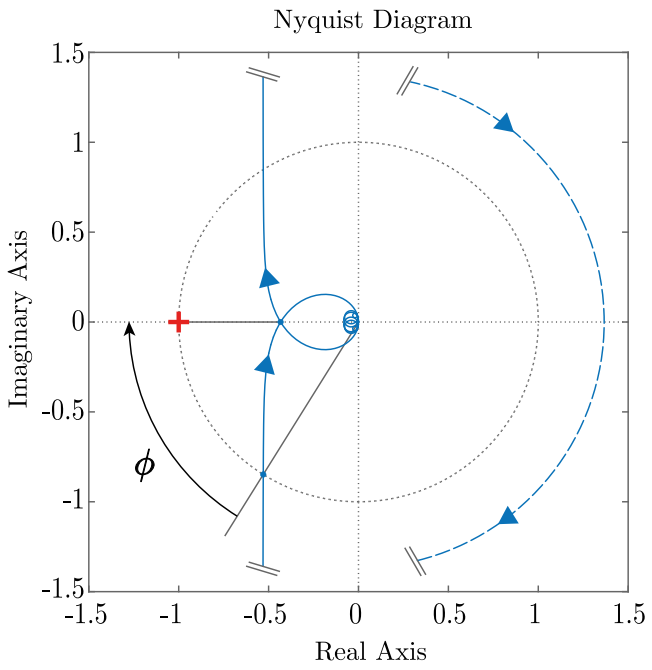

Fig. 7. Nyquist diagram of the closed-loop response of the integer-order controllers.

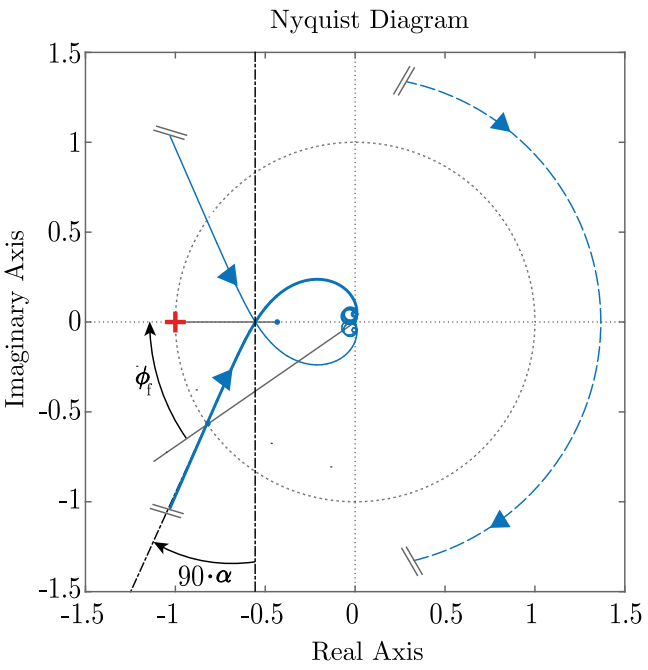

Fig. 8. Nyquist diagram of the fractional-order controller.

the time performance of the closed-loop system when tracking these signals is critical.

Just by applying the final value theorem to the closed-loop system it can be seen that because of the single integration of the tracking controller, ramp signals cannot be followed without tracking error. The only way to track these signals without steady state error is to increase the order of the integral action above 1. The main problem with this approach is that adding a second integral action will rotate the Nyquist diagram showed in Fig. 7 90° clockwise so that the system would become unstable. A trade-off between time performance and relative stability can be achieved by using fractional-order integrators. By adding a fractional order integrator of degree α to the traditional tracking controller the system can follow ramp signals while keeping a significant phase margin, this is because the fractional-order integrator will rotate the Nyquist diagram an amount equal to $90 \cdot \alpha$ as showed in Fig. 8.

The main goal of this paper is to compare the performance both in terms of time-domain and bandwidth of the well-known classical controllers used in nanopositioning systems and their fractional-order counterparts in order to demonstrate that with a proper design of their parameters the fractional-order versions can achieve a wider bandwidth and a better time-response while keeping a behaviour robust enough to compensate nonlinear effects such as the hysteresis of the system

3.1. Integer-order design of classical controllers

In order to carry out a fair comparison between the classical integer-order regulators and the proposed fractional-order versions, the IRC, PPF and PVFP controller are designed by means of an optimization procedure where closed-loop frequency response is the maximization goal and, the closed-loop stability of the system and a flat band response contained in the ±2 dB band are considered as restrictions. By following this procedure the following regulators are obtained.

3.1.1. Integer-order IRC

The Integral Resonant Control (IRC) block diagram is shown in Fig. 9 where $G(s)$ is the plant, d is a feedthrough constant term that

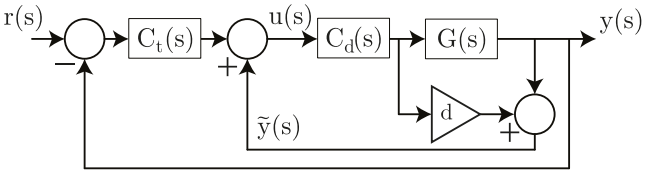

Fig. 9. Block diagram of the classical IRC control scheme.

together with $G_d(s)$ compose the damping controller and, $C_t(s)$ is the tracking controller. $C_d(s)$ is given by:

$$C_d(s) = \frac{k_d}{s}, \tag{4}$$

and $C_t(s)$ is an integral action given by:

$$C_t(s) = \frac{k_t}{s}, \tag{5}$$

After designing the parameters of the controller by following the aforementioned optimization procedure, the following regulator is obtained:

$$C_t(s) = \frac{729.47}{s}, \quad C_d(s) = \frac{7631.9}{s}, d = -0.88255. \tag{6}$$

This regulator leads to a theoretical value of closed-loop bandwidth equal to 533 Hz considering the ±3 dB criterion, it can be seen that this value is well above the 392 Hz obtained by using the expressions proposed in [39].

3.1.2. Integer-order PPF, PVPF and PAVPF

The Positive Position Feedback (PPF), Positive Velocity and Position Feedback (PVPF) and Positive Acceleration, Velocity and Position Feedback (PAVPF) share the same block diagram, showed in Fig. 10 where $G(s)$ is the plant, $G_d(s)$ is the damping controller and, $C_t(s)$ is the tracking controller. In the case of PPF $C_d(s)$ is given by:

$$C_d(s) = \frac{k_d}{s^2 + d_1 s + d_0}, \tag{7}$$

in the case of a PVPF controller is given by:

$$C_d(s) = \frac{n_1 s + n_0}{s^2 + d_1 s + d_0}. \tag{8}$$

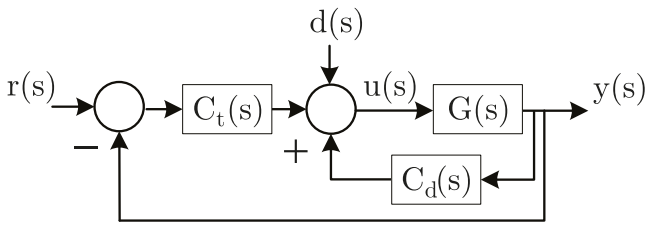

Fig. 10. The block diagram of the classical control schemes with damping and tracking approach, $G(s)$ is the nanopositioner, $C_d(s)$ is the damping controller, and $C_t(s)$ is the tracking controller.

and in the case of a PAVPF controller is given by:

$$C_d(s) = \frac{n_2 s^2 + n_1 s + n_0}{s^2 + d_1 s + d_0}. \tag{9}$$

In all the cases the tracking controller $C_t(s)$ has the same expression:

$$C_t(s) = \frac{k_t}{s}, \tag{10}$$

After designing the parameters of both controllers, the following regulators were obtained. In the case of the PPF controller:

$$\begin{aligned} C_t(s) &= \frac{1575.5}{s}, \\ C_d(s) &= \frac{43998400}{s^2 + 12670s + 3.934 \cdot 10^7}, \end{aligned} \tag{11}$$

in the case of the PVPF controller:

$$\begin{aligned} C_t(s) &= \frac{4060.9}{s}, \\ C_d(s) &= \frac{-16381s + 2.511 \cdot 10^7}{s^2 + 7288s + 5.534 \cdot 10^7}. \end{aligned} \tag{12}$$

and, in the case of the PAVPF controller:

$$\begin{aligned} C_t(s) &= \frac{5494.2}{s}, \\ C_d(s) &= \frac{-0.6385s^2 - 2.36 \cdot 10^4 s + 5.912 \cdot 10^6}{s^2 + 7578s + 6.258 \cdot 10^7}. \end{aligned} \tag{13}$$

These regulator lead to a theoretical value of closed-loop bandwidth equal to 729 Hz, 1133 Hz and 1240 Hz respectively. Again it can be seen that the results obtained by the optimization procedure are well above the ones obtained by using the expressions proposed in [39], 612 Hz and 738 Hz respectively.

In order to carry out a fair comparison between the classical integer-order regulators and the fractional-order versions the values of bandwidth obtained by using the optimization method will be used as baseline for the comparison.

4. Fractional-order design of classical controllers

As stated in Section 3 the main goal of the fractional-order version of the regulators is to increase the order of the integral action that all the controllers share in common for the tracking controller $C_t(s)$, however, this is not the only transfer function were a fractional exponent can be applied. To this point is important to note that by adding more parameters to the transfer function more degrees of freedom are added to the system in terms of design but more complexity is added in terms of design rules and practical implementation. The four controllers are designed with identical specifications in mind: maximize the closed-loop bandwidth whereas keeping the integral action of the tracking controller with a fractional-order exponent equal to 1.1 to provide a sufficient phase margin to the closed-loop system. This value was selected for the fractional-order exponent because the smaller phase margin of all the proposed integer-order regulators (worst case scenario) was 49.1°, considering the classical suggestion for closed-loop systems is of 45 degrees (critically damped), we allowed for a slightly smaller phase margin (40°) to achieve a trade-off between speed of response and maximally flat band response. With this value all the control schemes were guaranteed to have at least a value of 40° of phase margin. After applying this design criteria, the following transfer functions are proposed in this paper as fractional-versions of the classical controllers:

4.1. Fractional-order IRC

All the fractional-order regulators share the same block diagram as their integer-order counterparts, but the damping and tracking controllers of the fractional-order IRC (FOIRC) are given by the following expressions:

$$C_t(s) = \frac{k_t}{s^{(1+\alpha)}}, \quad C_d(s) = \frac{k_d}{s^{\beta}}, d. \tag{14}$$

It can be seen from (14) that this new regulator presents two additional degrees of freedom in the form of fractional exponents α and β. After designing the controller the following parameters were obtained:

$$C_t(s) = \frac{3105.2}{s^{1.1}}, \quad C_d(s) = \frac{1845.9}{s^{0.9}}, d = -1.1629. \tag{15}$$

4.2. Fractional-order PPF

The Fractional-order PPF (FOPPF) damping and tracking controllers' are given by the following expressions:

$$C_t(s) = \frac{k_t}{s^{(1+\alpha)}}, \quad C_d(s) = \frac{k_d}{s^{2\beta} + d_1 s^{\beta}}, \tag{16}$$

It can be seen from (16) that this new regulator presents again two additional degrees of freedom in the form of fractional exponents α and β. After designing the controller the following parameters were obtained:

$$\begin{aligned} C_t(s) &= \frac{3953}{s^{1.1}}, \\ C_d(s) &= \frac{25089600}{s^{2.0378} + 7646.8s^{1.0189} + 2.5296 \cdot 10^7}, \end{aligned} \tag{17}$$

4.3. Fractional-order PVPF

The Fractional-order PVPF (FOPVPF) damping and tracking controllers' are given by the following expressions:

$$C_t(s) = \frac{k_t}{s^{(1+\alpha)}}, \quad C_d(s) = \frac{n_1 s^{\tau} + n_0}{s^{2\beta} + d_1 s^{\beta}}, \tag{18}$$

It can be seen from (18) that this new regulator presents three additional degrees of freedom in the form of fractional exponents α, β and τ. After designing the controller the following parameters were obtained:

$$\begin{aligned} C_t(s) &= \frac{13451}{s^{1.1}}, \\ C_d(s) &= \frac{-156816s^{0.85001} + 3494112}{s^{2.0166} + 8924.3s^{1.0083} + 1.1169 \cdot 10^8}, \end{aligned} \tag{19}$$

4.4. Fractional-order PAVPF

The Fractional-order PAVPF (FOPAVPF) damping and tracking controllers' are given by the following expressions:

$$C_t(s) = \frac{k_t}{s^{(1+\alpha)}}, \quad C_d(s) = \frac{n_2 s^{2\tau} + n_1 s^{\tau} + n_0}{s^{2\beta} + d_1 s^{\beta}}, \tag{20}$$

It can be seen from (20) that this new regulator presents three additional degrees of freedom in the form of fractional exponents α, β and τ. After designing the controller the following parameters were obtained:

$$\begin{aligned} C_t(s) &= \frac{12532}{s^{1.1}}, \\ C_d(s) &= \frac{-1.7486s^{1.7807} - 177268s^{0.89037} + 7.0582 \cdot 10^5}{s^{2.0818} + 12835s^{1.0409} + 188884800}, \end{aligned} \tag{21}$$

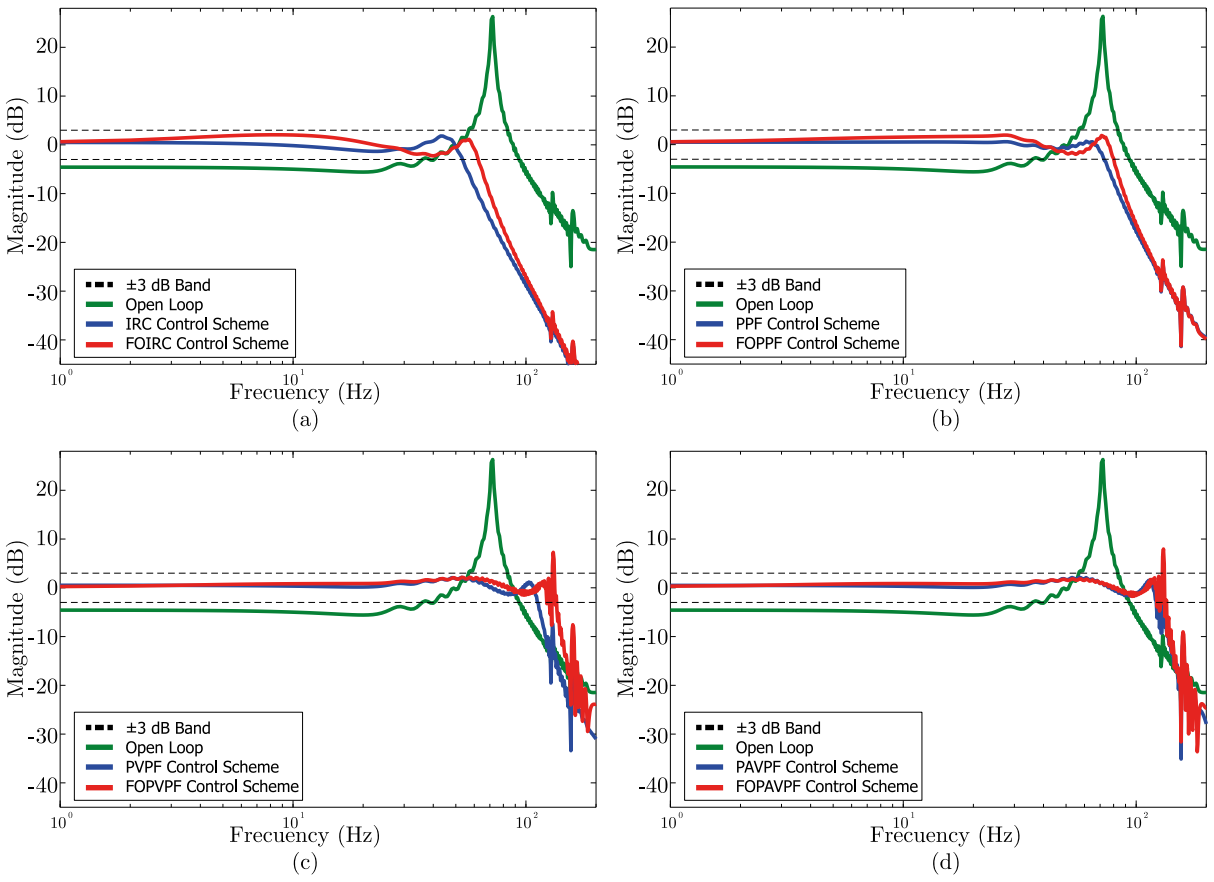

Fig. 11. Magnitude response of the nanopositioning platform, open-loop response and comparison between integer-order and fractional-order controllers in the case of (a) IRC, (b) PPF, (c) PVPF and, (d) PAVPF.

5. Verification of the controllers' performance

This section presents numerical and experimental results to demonstrate the effectiveness and advantages of the proposed fractional-order controllers over their integer-order counterparts.

The controllers utilized in this study were designed in the preceding sections. It is important to note that these four controllers were designed for the linear scenario, that is, without hysteresis, taking into account only the first resonant mode, and with identical specifications. In this section the simulated experiments on recorded data will be carried out considering a system with four modes of vibration and hysteresis in order to study the robustness of the control techniques considered to non-linear effects and modelling uncertainties. Both the frequency and the time response of these controllers will be checked.

The numerical implementation of the fractional expression in the transfer function that corresponds to the tracking action of all the controllers is implemented using the following expression:

$$C_t(s) = \frac{K_t}{s^{1+\alpha}} = \frac{K_t}{s^2} s^{\gamma} \tag{22}$$

where $\gamma = 1 - \alpha$. The fractional order differential operator of this expression is discretized by using the Grünwald–Letnikov (GL) definition of the discretized fractional operator [40], and the short memory approximation [41], as follows:

$$y_c(t) = T_s^{\gamma} \sum_{j=0}^{N-1} (-1)^j \binom{\gamma}{j} f(t - jT_s); \tag{23}$$

where the integral of the error signal $(r - y)$ multiplied by K_t, is the input to the block s^{γ}, $y_c(t)$ is its output, $N = 400$ is the number of terms involved in the discrete convolution, T_s is the sampling time, and the generalization of the combinatorial has been extended as follows:

$$\binom{\gamma}{j} = \frac{\gamma(\gamma+1)...(\gamma-j+1)}{j!}. \tag{24}$$

5.1. Frequency-domain results

To compare the performance and the sensitivity to high frequency disturbances of both the integer-order and fractional-order controllers the ±3 dB bandwidth criterion is used. It can be seen from the results displayed in Fig. 11 that in all the cases, the fractional-order implementation of the controllers exhibit a wider bandwidth at the expense of experiencing slight distortion in the high-frequency region, where it can be observed that the response ceases to be flat. This translates to a greater susceptibility to high-frequency disturbances and increased distortion in tracking very high-frequency references.

5.2. Time-domain results

Additionally to the results obtained in the frequency-domain, the time domain performance of the controllers are quantified by comparing the tracking capabilities of ramp-like signals where a triangular signal of 35 Hz is used as reference.

It can be seen from the results displayed in Fig. 12 that in all the cases, the fractional-order implementation of the controllers provides a smaller tracking error of ramp signals. This is outcome could be easily predicted as (1) the exponent of the tracking action is greater than one, (2) then bandwidth of the fractional-order controllers is bigger so they can track relatively low frequency signals with lower distortion than their integer-order counterparts.

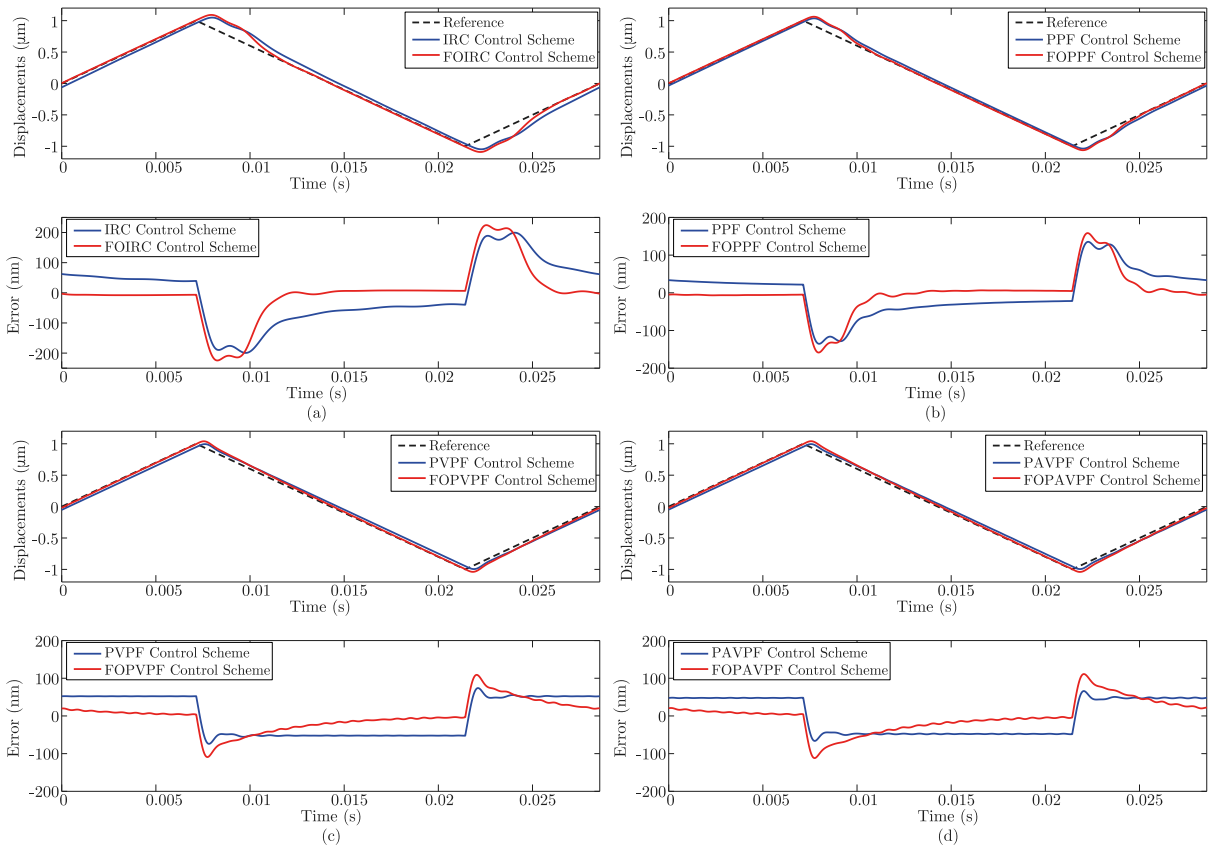

Fig. 12. Closed-loop system response and error for a triangular input waveform of frequency, 35 Hz, and amplitude, 1 μm. Comparison between integer-order and fractional-order controllers in the case of (a) IRC, (b) PPF, (c) PVPF and, (d) PAVPF.

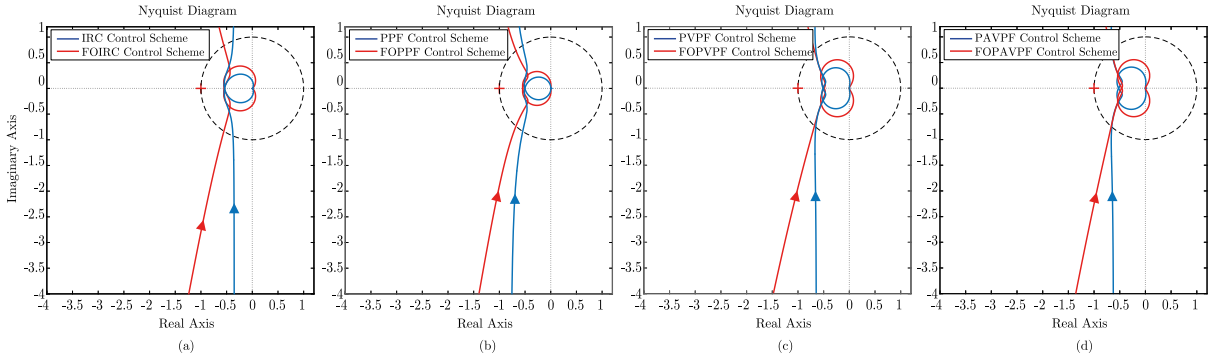

Fig. 13. Nyquist diagram of the closed-loop response of the system with integer-order and fractional order controllers in the case of (a) IRC, (b) PPF, (c) PVPF and, (d) PAVPF.

5.3. Discussion

The results obtained in the two previous sections are compared and discussed as follows.

1. The reduction of the phase margin for the fractional-order version of the three classical controllers is very small. This is because the design procedure that, by choosing the exponent of tracking controller equal to 1.1, guarantees that the phase margin and its asymptote are rotated $90° \cdot \alpha$ clockwise as showed in Fig. 13. The high value of phase margin makes the closed-loop system robust against effects that were neglected when designing the regulator such as hysteresis and high order vibration modes.
2. The robustness of the proposed controllers can be seen in the results obtained in Section 5 where all the results were obtained considering hysteresis and four modes of vibration in the system. The controllers always remain stable and the closed-loop bandwidth is not significantly reduced.
3. The fractional-order version of the controllers present a better performance in terms of the time response of the system, as the tracking error of ramp-like signals is much smaller than the integer-order version of the controllers. This behaviour is quantified by means of the Integral Square Error (ISE) depicted in Table 2.

The classical performance indices of the six controllers analysed in this paper are summarized in Table 2.

The phase and gain margins, offering crucial insights into the relative stability of the nominal system, fall within the ranges of $[47.4°, 67.9°]$ for the phase margin and $[5.25, 6.72]$dB for the gain margin. Notably, the phase margin aligns with the classical suggestion

Table 2
Performance indices of the integer-order and fractional-order control schemes.

Controller	IRC	FOIRC	PPF	FOPPF	PVPF	FOPVPF	PAVPF	FOPAVPF
±3 dB Bandwidth (Hz)	530	620	720	800	1120	1230	1220	1230
ISE ($\cdot 10^{-4}$)	5.25	3.42	1.68	1.18	0.78	0.44	0.65	0.49
Phase margin (°)	67.9	56.5	56.7	47.4	49.1	47.2	49.1	48.2
Gain margin (dB)	5.36	5.25	5.92	5.27	5.82	6.20	5.63	6.72
Vector margin	0.46	0.45	0.49	0.45	0.47	0.47	0.46	0.49

for fractional-order closed-loop systems [42], falling within the recommended range of $[45°, 60°]$. Gain margin represents the pure gain that can be added to the loop before system instability, and Table 2 indicates that all controllers can accommodate substantial gain increases without compromising stability.

Furthermore, Table 2 includes the vector margin, defined as the distance to the −1 point from the closest approach of the Nyquist plot of the loop gain (refer to Fig. 13). The vector margin, as a singular margin parameter, eliminates ambiguities associated with combining gain margin and phase margin. Larger vector margins indicate better stability robustness, and in this case, none of the fractional-order implementations of the proposed controllers compromise the vector margin significantly. The maximum reduction in the vector margin is only 0.04, observed when implementing the FOPPF.

Lastly, the data in Table 2 underscores that fractional-order regulators outperform their integer-order counterparts in both bandwidth and tracking ramp-like signals. This is achieved with only a marginal reduction in phase margin (about 10° in the worst case), maintaining the robustness to uncertainties characteristic of classical controllers. This aligns with expectations, as demonstrated in [43,44], where it was asserted that the use of a fractional-order regulator helps maintain a nearly constant phase margin and indirectly reduces damping variation for significant changes in the frequency of the first vibration mode, thus enhancing the system's robustness to uncertainties or parameter variations.

6. Conclusion

The closed-loop positioning performance of fractional-order implementations of four classical control schemes popularly employed in nanopositioning applications namely: FOIRC, FOPPF, FOPVPF and FOPAVPF, has been thoroughly compared with their integer-order counterparts. Due to the additional degree of freedom in design parameters afforded by the fractional-order controllers achievable closed loop positioning bandwidth is increased, while maintaining a flat pass-band response. Simulated experiments on recorded data show an enhancement of the overall performance of the fractional-order controllers when compared with their integer-order implementations even in the presence of unmodelled nonlinear effects such as hysteresis. The achievable bandwidth is increased by up to 17% and the positioning accuracy is significantly increased (ISE reduced by up to 35%). With high-speed, precise nanopositioning for complex trajectories being aimed for in several emerging applications, fractional-order implementations of classical control schemes and novel fractional-order control schemes must be further explored to exploit their untapped potential to deliver significant closed-loop performance improvements.

Declaration of competing interest

The authors declare that they have no known competing financial interests or personal relationships that could have appeared to influence the work reported in this paper.

References

[1] Gu G-Y, Zhu L-M, Su C-Y, Ding H, Fatikow S. Modeling and control of piezo-actuated nanopositioning stages: A survey. IEEE Trans Autom Sci Eng 2016;13(1):313–32. http://dx.doi.org/10.1109/TASE.2014.2352364.

[2] Rana MS, Pota HR, Petersen IR. Improvement in the imaging performance of atomic force microscopy: A survey. IEEE Trans Autom Sci Eng 2017;14(2):1265–85. http://dx.doi.org/10.1109/TASE.2016.2538319.

[3] Lin F-J, Lee S-Y, Chou P-H. Computed force control system using functional link radial basis function network with asymmetric membership function for piezo-flexural nanopositioning stage. IET Control Theory Appl 2013;7(18):2128–42. http://dx.doi.org/10.1049/iet-cta.2013.0086.

[4] Xu Q. Enhanced discrete-time sliding mode strategy with application to piezoelectric actuator control. IET Control Theory Appl 2013;7(18):2153–63. http://dx.doi.org/10.1049/iet-cta.2013.0361.

[5] Xu Q, Cao Z. Piezoelectric positioning control with output-based discrete-time terminal sliding mode control. IET Control Theory Appl 2017;11(5):694–702. http://dx.doi.org/10.1049/iet-cta.2016.0956.

[6] Hong Z, Tang H, Xu Y, Wu Z, Li J. A new high-bandwidth nanopositioning tracking control method with input shaper and integral resonance controller. Proc CIRP 2020;89:182–8. http://dx.doi.org/10.1016/j.procir.2020.05.140.

[7] Tao Y, Li L, Li H-X, Zhu L. High-bandwidth tracking control of piezoactuated nanopositioning stages via active modal control. IEEE Trans Autom Sci Eng 2021;19:2998–3006.

[8] Devasia S, Eleftheriou E, Moheimani SOR. A survey of control issues in nanopositioning. IEEE Trans Control Syst Technol 2007;15(5):802–23. http://dx.doi.org/10.1109/TCST.2007.903345.

[9] Rana MS, Pota HR, Petersen IR. A survey of methods used to control piezoelectric tube scanners in high-speed AFM imaging. Asian J Control 2018;20(4):1379–99. http://dx.doi.org/10.1002/asjc.1728.

[10] Fanson JL, Caughey TK. Positive position feedback control for large space structures. AIAA J 1990;28(4):717–24. http://dx.doi.org/10.2514/3.10451.

[11] Bhikkaji B, Ratnam M, Moheimani S. PVPF control of piezoelectric tube scanners. Sensors Actuators A 2007;135(2):700–12. http://dx.doi.org/10.1016/j.sna.2006.07.032.

[12] Aphale SS, Fleming AJ, Moheimani SOR. Integral resonant control of collocated smart structures. Smart Mater Struct 2007;16(2):439–46. http://dx.doi.org/10.1088/0964-1726/16/2/023.

[13] Li L, Li C-X, Gu G, Zhu L-M. Positive acceleration, velocity and position feedback based damping control approach for piezo-actuated nanopositioning stages. Mechatronics 2017;47:97–104. http://dx.doi.org/10.1016/j.mechatronics.2017.09.003.

[14] Feng H, Pang A, Zhou H. High precision robust control design of piezoelectric nanopositioning platform. Sci Rep 2022;12(1):10357. http://dx.doi.org/10.1038/s41598-022-14332-5.

[15] Li L, Aphale SS, Zhu L. High-bandwidth nanopositioning via active control of system resonance. Front Mech Eng 2021;16(2):331–9. http://dx.doi.org/10.1007/s11465-020-0619-x.

[16] Russell D, San-Millan A, Feliu V, Aphale SS. Butterworth pattern-based simultaneous damping and tracking controller designs for nanopositioning systems. Front Mech Eng 2016;2. http://dx.doi.org/10.3389/fmech.2016.00002.

[17] Behera P, Dey A, Patra S. Control of negative imaginary systems exploiting a dissipative characterization. Automatica 2022;146:110634. http://dx.doi.org/10.1016/j.automatica.2022.110634.

[18] San-Millan A, Feliu-Batlle V, Aphale SS. Fractional order implementation of Integral Resonant Control – A nanopositioning application. ISA Trans 2018;82:223–31. http://dx.doi.org/10.1016/j.isatra.2017.09.022, Fractional Order Signals, Systems, and Controls: Theory and Application.

[19] Xu R, Wang Z, Zhou M, Tian D. A robust fractional-order sliding mode control technique for piezoelectric nanopositioning stages in trajectory-tracking applications. Sensors Actuators A 2023;363:114711. http://dx.doi.org/10.1016/j.sna.2023.114711.

[20] Feng Z, Ming M, Ling J, Xiao X, Yang Z-X, Wan F. Fractional delay filter based repetitive control for precision tracking: Design and application to a piezoelectric nanopositioning stage. Mech Syst Signal Process 2022;164:108249. http://dx.doi.org/10.1016/j.ymssp.2021.108249.

[21] Sabatier J, Lanusse P, Melchior P, Oustaloup A. Fractional order differentiation and robust control design: CRONE, h-infinity and motion control. Intelligent systems, control and automation: science and engineering, Springer Netherlands; 2015.

[22] Krijnen ME, van Ostayen RA, HosseinNia H. The application of fractional order control for an air-based contactless actuation system. ISA Trans 2018;82:172–83. http://dx.doi.org/10.1016/j.isatra.2017.04.014, Fractional Order Signals, Systems, and Controls: Theory and Application.
[23] Marinangeli L, Alijani F, HosseinNia SH. Fractional-order positive position feedback compensator for active vibration control of a smart composite plate. J Sound Vib 2018;412:1–16. http://dx.doi.org/10.1016/j.jsv.2017.09.009.
[24] HosseinNia SH, Saikumar N. Fractional-order precision motion control for mechatronic applications. De Gruyter; 2019, http://dx.doi.org/10.1515/9783110571745-015.
[25] Kapoulea S, Psychalinos C, Elwakil AS. Double exponent fractional-order filters: Approximation methods and realization. Circuits Systems Signal Process 2021;40(2):993–1004. http://dx.doi.org/10.1007/s00034-020-01514-7.
[26] Tepljakov A, Alagoz BB, Yeroglu C, Gonzalez EA, Hosseinnia SH, Petlenkov E, et al. Towards industrialization of FOPID controllers: A survey on milestones of fractional-order control and pathways for future developments. IEEE Access 2021;9:21016–42. http://dx.doi.org/10.1109/ACCESS.2021.3055117.
[27] Monje CA, Vinagre BM, Feliu V, Chen Y. Tuning and auto-tuning of fractional order controllers for industry applications. Control Eng Pract 2008;16(7):798–812. http://dx.doi.org/10.1016/j.conengprac.2007.08.006.
[28] Tavazoei MS, Tavakoli-Kakhki M. Compensation by fractional-order phase-lead/lag compensators. IET Control Theory Appl 2014;8(5):319–29. http://dx.doi.org/10.1049/iet-cta.2013.0138.
[29] Monje C, Ramos F, Feliu V, Vinagre B. Tip position control of a lightweight flexible manipulator using a fractional order controller. IET Control Theory Appl 2007;1:1451–60.
[30] Bohannan GW. Analog fractional order controller in temperature and motor control applications. J Vib Control 2008;14(9–10):1487–98. http://dx.doi.org/10.1177/1077546307087435.
[31] Feliu-Talegon D, San-Millan A, Feliu-Batlle V. Fractional-order integral resonant control of collocated smart structures. Control Eng Pract 2016;56:210–23. http://dx.doi.org/10.1016/j.conengprac.2016.07.016.
[32] Li L-L, Gu G-Y, Zhu L-M. A fractional-order active damping control approach for piezo-actuated nanopositioning stages. In: 2016 international conference on manipulation, automation and robotics at small scales. 2016, p. 1–6. http://dx.doi.org/10.1109/MARSS.2016.7561707.
[33] San-Millan A, Feliu-Batlle V, Aphale SS. Application of a fractional order integral resonant control to increase the achievable bandwidth of a nanopositioner. IFAC-PapersOnLine 2017;50(1):14539–44. http://dx.doi.org/10.1016/j.ifacol.2017.08.2079, 20th IFAC World Congress.
[34] Hanssen MA. Control in atomic force microscopy: A fractional order approach (Ph.D. thesis), Norwegian University of Science and Technology; 2019.
[35] Moltumyr AH, Ragazzon MR, Gravdahl JT. Fractional-order control: Nyquist constrained optimization. IFAC-PapersOnLine 2020;53(2):8605–12. http://dx.doi.org/10.1016/j.ifacol.2020.12.519, 21st IFAC World Congress.
[36] L. Y, Z. Z, Y. Z, D. L. Rate-dependent modeling of piezoelectric actuators for nano manipulation based on fractional Hammerstein model. Micromachines 2021;13(1):14. http://dx.doi.org/10.3390/mi13010042.
[37] Leang K, Zou Q, Devasia S. Feedforward control of piezoactuators in atomic force microscope systems. IEEE Control Syst Mag 2009;29(1):70–82. http://dx.doi.org/10.1109/MCS.2008.930922.
[38] Du J, Feng Y, Su C-Y, Hu Y-M. On the robust control of systems preceded by coleman-hodgdon hysteresis. In: 2009 IEEE international conference on control and automation. 2009, p. 685–9. http://dx.doi.org/10.1109/ICCA.2009.5410229.
[39] Russell D, San-Millan A, Feliu V, Aphale SS. Butterworth pattern-based simultaneous damping and tracking controller designs for nanopositioning systems. Front Mech Eng 2016;2. http://dx.doi.org/10.3389/fmech.2016.00002.
[40] Vinagre BM, Podlubny I, Hernandez A, Feliu V. Some approximations of fractional order operators used in control theory and applications. Fract Calc Appl Anal 2000;3(3):231–48.
[41] Podlubny I. Fractional differential equations: an introduction to fractional derivatives, fractional differential equations, to methods of their solution and some of their applications, vol. 198, Academic Press; 1998.
[42] Monje CA, Vinagre BM, Feliu V, Chen Y. Tuning and auto-tuning of fractional order controllers for industry applications. Control Eng Pract 2008;16(7):798–812. http://dx.doi.org/10.1016/j.conengprac.2007.08.006.
[43] Monje C, Ramos F, Feliu V, Vinagre B. Tip position control of a lightweight flexible manipulator using a fractional order controller. IET Control Theory Appl 2007;1. 1451–1460(9).
[44] Feliu-Talegon D, Feliu-Batlle V. Passivity-based control of a single-link flexible manipulator using fractional controllers. Nonlinear Dynam 2019;95:2415–41.